

A mesoscale mechanical model of cellular interactions

Kathleen T. DiNapoli,¹ Douglas N. Robinson,¹ and Pablo A. Iglesias^{1,2,*}

¹Department of Cell Biology, Johns Hopkins University School of Medicine, Baltimore, Maryland and ²Department of Electrical & Computer Engineering, Johns Hopkins University Whiting School of Engineering, Baltimore, Maryland

ABSTRACT Computational models of cell mechanics allow the precise interrogation of cell shape change. These morphological changes are required for cells to survive in diverse tissue environments. Here, we present a mesoscale mechanical model of cell-substrate interactions using the level set method based on experimentally measured parameters. By implementing a viscoelastic mechanical equivalent circuit, we accurately model whole-cell deformations that are important for a variety of cellular processes. To effectively model shape changes as a cell interacts with a substrate, we have included receptor-mediated adhesion, which is governed by catch-slip bond behavior. The effect of adhesion was explored by subjecting cells to a variety of different substrates including flat, curved, and deformable surfaces. Finally, we increased the accuracy of our simulations by including a deformable nucleus in our cells. This model sets the foundation for further exploration into computational analyses of multicellular interactions.

SIGNIFICANCE Morphological change and appropriate adhesion are necessary for the survival and behavior of cells in tissue environments. To interrogate the role of cell mechanics and adhesion in these cellular interactions, we have implemented a computational model of cell shape change. Here, we introduce cell-substrate interactions using the level set method (LSM). This model includes an experimentally measured parameter set describing cell mechanics, interactions with solid and deformable substrates, receptor-mediated adhesion, and incorporation of a deformable nucleus. This LSM framework provides the foundation for precision modeling of cell mechanics, allowing testing of how the modulation of mechanics impacts cell behavior in complex multicellular environments. This framework will facilitate the ability to explain and predict the behavior of healthy and diseased multicellular systems.

INTRODUCTION

A cell's ability to change shape and interact with its environment is essential for growth, proliferation, tracking and consuming nutrients, and survival. In single-cell and multicellular systems, a variety of morphological changes are required for cells to interact with other cells and their local environment. Cell consumption events such as phagocytosis, entosis, endocytosis, and micropinocytosis all are characterized by a cell deformation in which external materials, including nutrients, media, particles, or other cells, are engulfed. These events represent a diverse array of biological processes that are present across a wide range of cell types. The mechanical properties of these cell engulfment processes are well characterized and therefore provide a

good basis to begin interrogating multicellular interactions through the reduced computational requirements of the two-cell scenarios.

Simulating cell engulfment events requires considering cellular interactions and understanding how cells adhere to these surfaces, which include the substrate or neighboring cells. Cell-cell interactions can be modeled at various length scales, from subcellular simulations considering interactions of individual receptors that enable cell adhesion (1,2) to tissue-level simulations representing hundreds of cells (3,4). To accomplish modeling across these ranges of complexity requires a variety of different computational techniques. Here, we consider a mesoscale-scale model involving simulations of one to two cells with a focus on recreating the corresponding cell shape changes. Many techniques are available for modeling deformable cells with high geometric resolution (5). Most of these have been used to simulate migration (6–9), although some have been used in other biological processes such as cell division

Submitted May 7, 2021, and accepted for publication October 18, 2021.

*Correspondence: pi@jhu.edu

Editor: Dimitrios Vavylonis.

<https://doi.org/10.1016/j.bpj.2021.10.021>

© 2021 Biophysical Society.



(10–12) and phagocytosis (13). We implement our approach using the level set method (LSM), which was originally developed to represent interactions across phases and can track moving boundaries accurately.

Though the LSM has been successfully used to simulate various cellular processes that involve individual deformable cells (10,14,15), to our knowledge it has not been previously used to interrogate cell-substrate contacts or cell-cell interactions such as engulfment. To incorporate these phenomena, which involve receptor-mediated adhesions, requires that we consider a model for these adhesions. Our implementation assumes that adhesions arise from catch-slip bonds. Catch-slip bonds are characterized by having biphasic behavior depending on the force applied. During the catch phase, the dissociation decreases transiently as the strength of the tensile force increases (16,17). In contrast, during the slip phase, after sufficient tensile force has been applied to the bond, the rate of dissociation increases. These can be represented mathematically as in the Bell model (18). Many catch-slip proteins such as cadherins are necessary for healthy cell development, migration, and physiology (19,20).

In this study, we begin by briefly describing the implementation of the LSM for deformable cells, followed by a description of how active stresses and adhesion are implemented in this framework with both solid and deformable substrates. The model is first tested with cells interacting with flat solid substrates to verify the implementation of adhesion. We then explore the landscape of more biologically relevant cell engulfment events through modulation of mechanical parameters and stress production. We further increase the biological accuracy of these simulations through the introduction of a mechanically deformable nucleus. Ultimately, this model lays the foundation to understand better the mechanistic details of cellular interactions and cell consumption events and to predict cell behavior across different scenarios.

MATERIALS AND METHODS

Model overview

A cell's shape is affected by a variety of different mechanical parameters that are specific to the cell type as well as its environment. We considered a range of physical processes, which include experimentally measured physical parameters such as cortical tension and viscoelasticity as well as various active and passive stresses (Fig. 1 A; Table 1). Cortical tension is the energy cost for adding a unit of surface area to the cell (21). Cortical tension, along with the local curvature of the cell, creates a Laplace-like pressure that drives the cell to minimize the surface area/volume ratio. Additionally, the viscoelasticity of the cell is determined by the components of the cytoskeletal network, which provide a time-dependent response to stresses imposed (22). We represented the cellular viscoelasticity with a mechanical equivalent circuit representing the cell cortex and membrane (Kelvin-Voigt) in series with a purely viscous cytoplasm (Fig. 1 B). The resulting cell shape is determined by the balance of stresses. These stresses range from the small stochastic membrane fluctuations (Fig. 1 C) that contribute to cell adhesion to active stresses driven by actin polymerization

and myosin contractility to several passive stresses, such as the propensity to conserve cellular volume and the Laplace-like pressure described above (Fig. 1 D). We include adhesion between the cell and its environment, which can be either an extracellular matrix or a neighboring cell.

Implementing the LSM

The LSM is a numerical technique that tracks the evolution of an interface with high geometric accuracy while improving computational efficiency by defining boundaries on a fixed Cartesian grid and eliminating the need for parameterization (24). Originally developed to simulate propagating fronts with curvature-dependent speeds (31,32), the LSM has been used in various biological settings (5). Here, we highlight some of the basics; a detailed description of the LSM implementation in modeling cells is provided in (24).

The LSM uses an implicit scheme to define arbitrary surfaces. The cellular boundary, $\Gamma(t)$, is defined as the zero-level isocontour of potential function $\phi(z, t)$, defined as one dimension higher than $\Gamma(t)$. In our simulations, $z = (x, y) \in \mathbb{R}^2$; this renders a two-dimensional (2D) simulation representing a cross section through the cell. Though several possibilities exist for choosing $\Gamma(t)$, there are numerical advantages to choosing a signed distance function to describe the potential function $\phi(z, t)$ (33). In particular, the distance from point z to the boundary $\Gamma(t)$ is described by

$$\phi(z, t) = \pm \min_{z^* \in \Gamma(t)} \|z - z^*\|,$$

where the sign is +1 for points outside of the boundary and −1 for points inside. Throughout the evolution of the simulation, if the boundary deviates from the signed distance function (the normal of the gradient of ϕ is greater than a defined parameter threshold), it can be reinitialized using the function

$$\frac{\partial \phi}{\partial t} + \text{sign}(\phi)(\|\nabla \phi\| - 1) = 0.$$

In simulations in which cells undergo significant deformations or experience significant stresses, reinitialization was required more frequently.

Inclusion of stresses in LSM

The evolution of ϕ is described by the equation

$$\frac{\partial \phi}{\partial t} + v \cdot \nabla \phi = 0,$$

where v describes the local velocity of the potential function. To calculate the velocity, we first compute the various stresses acting on the cell and use a viscoelastic mechanical equivalent circuit of the cell to determine their effect on the local velocity. The velocity of the cell is then given by $v(z, t) = \partial x_{\text{bound}} / \partial t$, where x_{bound} takes into account the deformation of the cytoplasm and cortex, as described below (Eq. 5). As per the level set formalism, the total stresses acting on the cell (σ_{tot}) are applied outward or inward normal to the cell boundary and include passive and active stresses.

We consider two passive stresses:

$$\sigma_{\text{passive}} = \sigma_{\text{ten}} + \sigma_{\text{area}}.$$

Surface tension (σ_{ten}) captures the Laplace-like pressure found at the interphase between the cell and its environment; it is given by

$$\sigma_{\text{ten}} = \gamma_{\text{ten}} \kappa(z, t),$$

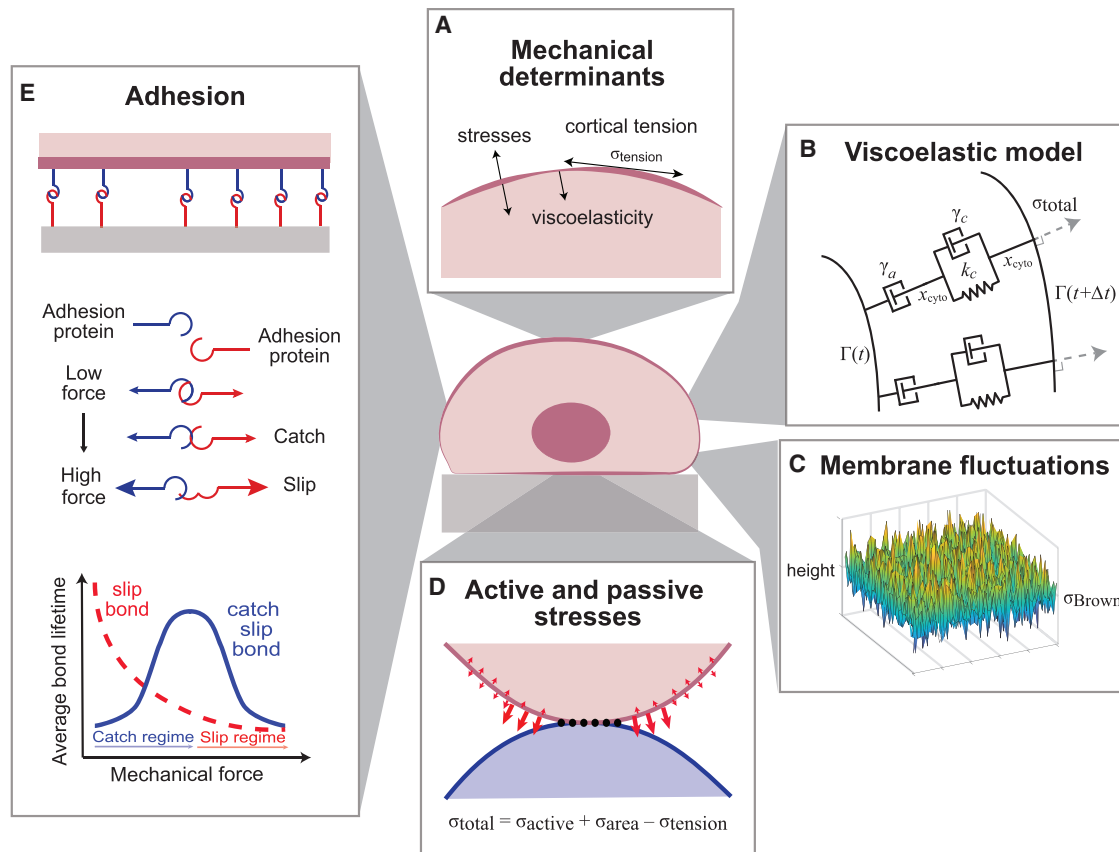


FIGURE 1 Elements of cell shape change.

For a Figure360 author presentation of this figure, see <https://doi.org/10.1016/j.bpj.2021.10.021>

A combination of components determines a cell's shape over time. (A) The effective cortical tension and viscoelasticity are cell type specific and can be measured experimentally. These mechanical parameters (among others) determine the degree of cellular deformation in response to stress (externally applied or internally generated). (B) These stresses are applied to our mechanical equivalent circuit at all points along the level set function to determine the shape $\Gamma(t)$. This viscoelastic mechanical circuit models the cell as a compound material consisting of a mostly viscous cytoplasm (γ_a) and a viscoelastic cell membrane/cortex (γ_c, k_c). The amount that the boundary deforms because of the total stress acting on the system (x_{cyto}, x_{cort}) is determined by the mechanical constants populating the model. (C) Brownian fluctuations of the membrane represent small displacements away from the mean state. These stochastic fluctuations are included in the total stresses acting on the system. (D) These deformations are determined based on a combination of multiple stresses, including the active stresses (σ_{active}) and stresses to conserve volume/area (σ_{area}) and curvature (σ_{ten}). Small arrows represent the distribution of Brownian fluctuations, and large arrows indicate active force production. (E) We consider adhesion at points of contact. Adhesion is modeled as a catch-slip bond that can be exemplified by E-cadherins, among others. The lifetime of these bonds has a force dependency whereby bond lifetime increases transiently under a moderate mechanical load (catch regime) but enters the slip regime once the mechanical load becomes sufficiently large, ultimately leading to bond breakage. We treat this behavior as location dependent using an adaptation of the Bell model (18,23). To see this figure in color, go online.

where γ_{ten} is the local cortical tension, $\kappa = \nabla \cdot \mathbf{n}$ is the local curvature, and \mathbf{n} is the unit normal vector. We assume that the cytosol is incompressible, which implies that the cell volume remains constant. In this two-dimensional model of the cell, we enforce this by constraining the area enclosed by the cell boundary. To this end, we implement a stress given by

$$\sigma_{area} = \gamma_A(A(t) - A_0),$$

where $A(t)$ and A_0 are the areas enclosed by the cell boundary at times t and $t = 0$, and γ_A is a conservation term used to ensure that the cell's area does not change over the course of the simulation (Fig. S1). Note that we do not assume that the perimeter is conserved because *Dictyostelium* is known to shuttle membrane so that it is not limiting (34). When considering other cells, the perimeter could also be constrained in a similar manner.

The addition of active stresses,

$$\sigma_{active} = \sigma_{Brown} + \sigma_{pro} + \sigma_{ret},$$

increases local velocity, thereby displacing the cell membrane. Active stresses are a combination of Brownian motion (σ_{Brown}) due, in part, to thermal fluctuations at the membrane; protrusive stress (σ_{pro}), representing actin polymerization at the front end; and retractive stress (σ_{ret}), representing myosin contractility at the rear end. All stresses are applied as a vector normal to the boundary of the cell. Protrusive and retractive stresses are modeled deterministically; an example of their spatial distribution can be seen in Fig. S2. In our model, we do not explicitly model subcellular actomyosin concentrations or activity, nor do we consider how they may change over time in response to a mechanical stimulus (35,36). Instead, we apply active stresses based on the experimentally measured actomyosin force production at regions experiencing active protrusive or retractive stresses on predetermined regions of the cell

TABLE 1 Simulation parameters

| Parameter (symbol) | Value (units) | Reference |
|--------------------------------------|-------------------------|------------------------------------|
| Mechanical parameters | | |
| Cortical elasticity | k_c | 0.098 nN/ μm^3 (24) |
| Cortical viscosity | γ_c | 0.064 s · nN/ μm^3 (24) |
| Cytoplasmic viscosity | γ_a | 6.090 s · nN/ μm^3 (24) |
| Cortical tension | γ_{ten} | 0–1 nN/ μm^3 (24) |
| Protrusive stress | σ_{pro} | 1–6 nN/ μm^3 (25,26) |
| Brownian stress SD | σ_{Brown} | 55 pN/ μm^3 Computed |
| E-cadherin binding parameters | | |
| catch bond | ϕ_c | 13 pN (27) |
| slip bond | ϕ_s | 43 pN (27) |
| maximal bond | ϕ_{max} | 28 pN Computed |
| maximal bond density | N_t | 43 per μm^2 (27) |
| on rate | Γ | 5.3 s ⁻¹ our estimate |
| off rate | k_{off} | 1.6 s ⁻¹ (27) |
| attachment threshold | σ_{max} | 1.7 nN/ μm^2 Eq. 5 |
| P-selectin binding parameters | | |
| catch bond | ϕ_c | 5 pN (28) |
| slip bond | ϕ_s | 24 pN (28) |
| maximal bond | ϕ_{max} | 14.5 pN Computed |
| maximal bond density | N_t | 350 per μm^2 (29) |
| on rate | Γ | 1 s ⁻¹ our estimate |
| off rate | k_{off} | 1.4 s ⁻¹ (30) |
| attachment threshold | σ_{max} | 5.2 nN/ μm^2 Eq. 5 |

perimeter (Fig. S2). These values have been well quantified experimentally (25,26,22).

Initial cell-substrate contact can be initiated by stochastic contact through Brownian motion (Fig. 1 C). Observable membrane fluctuations can be caused by thermal noise and by underlying cellular activity driven by the cytoskeleton (37–40). When computing the magnitude of Brownian motion, we do not model temperature explicitly. Instead, we use experimental measurements of supported intermembrane junctions which suggest that a membrane fluctuates with a root mean-square displacement (Δx^2) of ~ 50 nm (41,42). To determine the stress required to produce these fluctuations, we worked backward. As shown in the supplemental file, the magnitude of the stress required to produce these fluctuations has a standard deviation given by

$$\sigma_{\text{Brown}} = \left(\frac{2k_c \gamma_c \Delta x^2}{dt} \right)^{1/2}. \quad (1)$$

We assume that these fluctuations primarily affect the membrane of the cell, which in our model is represented as the compound cortex (consisting of the membrane and underlying actomyosin cytoskeleton); therefore, only the Kelvin-Voigt element of the viscoelastic circuit was included in the calculation. The frequency with which the fluctuations occur varies as a function of the time step (dt) assigned for the simulation. The Brownian fluctuations (σ_{Brown}) are uniformly distributed across the entire cell membrane, and their magnitude at each point is recomputed at each iteration of the simulation to capture the stochasticity of the process. This, combined with the protrusive and retractive stresses (σ_{pro} , σ_{ret}), acts as the active stress (σ_{active}). The total stress (expressed in nanonewtons per square micron) is then given by

$$\sigma_{\text{tot}} = \sigma_{\text{passive}} + \sigma_{\text{active}}. \quad (2)$$

When only passive stresses are considered, they are sufficient to instigate contact between a cell and a substrate. When active stresses are added, these passive stresses become nearly negligible. At points of contact, the cell shape is also restricted to ensure that it remains excluded from the volume

of the interacting surface. This is done by constructing a mask potential function representing the shape of the surface with which the cell is interacting (43). At points at which the cell's potential function intersects the mask's potential function, the cell's shape is clipped by

$$\phi(t + \Delta t) = \min(\phi(t + \Delta t), \psi),$$

where ψ is the potential function of the mask. When considering two deformable cells, each exerting active σ , each cell applies a stress to the other proportional to the local velocity. The total stress for each cell is computed independently before applying a stress to the opposite. Specifically, if two cells, denoted 1 and 2, exert total stresses σ_{tot1} and σ_{tot2} , respectively, at a common contact point, then the net stress affecting cell 1 is given by

$$\sigma_{1-\text{net}} = \sigma_{\text{tot1}} - |\sigma_{\text{tot2}}|,$$

with a similar formula for the stress on cell 2.

Modeling a cell with a deformable nucleus

To model a cell with a deformable nucleus, a second level set function was used and was chosen so that initially, the nucleus was near the cell centroid. The nucleus was assumed to occupy 40–50% of the area of the cell, with elasticity ranging from 0.25 times to four times that of a wild-type cell. The nucleus is modeled as a viscoelastic material based on the same mechanical equivalence circuit shown in Fig. 1 B. In this way, we are not considering the more complex nuclear dynamics that occur after mechanical deformation (44,45). The outer cell membrane acts as a mask for the inner nucleus and is described as

$$\phi_1(t + \Delta t) = \max(\phi_1(t + \Delta t), \phi_2(t + \Delta t)),$$

where ϕ_1 and ϕ_2 are the potential functions for the nucleus and the cell, respectively. Masking prevents the nucleus from leaving the boundary of the cell membrane. As the outer cell deforms according to the velocity resulting from the total stress as defined by Eq. 2, the nucleus will move tracking the cell by modeling molecular linkages of the nucleus to the cytoskeleton as elastic springs following Hooke's law:

$$\sigma_{\text{link}} = k_{\text{Hooke}} \|z_1(t) - z_2(t)\|,$$

where $z_1(t) = (x_1(t), y_1(t))$ and $z_2(t) = (x_2(t), y_2(t))$ are the centroids of the nucleus and cell at time t , respectively, and k_{Hooke} is the Hooke constant. This term resulted in a biologically relevant stress regime of fewer than 2 nN/ μm^2 (46,47). This stress was applied as a Gaussian on the perimeter of the nucleus, with the maximal stress applied in the direction of motion. This, along with passive stresses (σ_{area} , σ_{ten}), allows the cell to move through space while the nucleus remains near the center of the cytoskeleton applying stress to the nucleus (47). If the cell has extended thin protrusions, as in cell engulfment events, we compute the location of the nuclear centroid by considering the centroid of the cell excluding the extended protrusions by

$$\sigma_{\text{link-net}} = \min(\sigma_{\text{link}}, D),$$

where D is the threshold of points to be included in the calculation of the point of maximal tension. The total stress acting on the nucleus acts on approximately half the cell in the direction of movement.

Inclusion of cell adhesion

We implement adhesion in the form of catch-slip bonds based on measured values for different cell-substrate and cell-cell adhesion proteins. From a

biomechanical perspective, these types of adhesion bonds may be incorporated somewhat generically based on a biophysically relevant stress landscape representing many adhesion proteins. Catch-slip bonds are force dependent, where at lower force, the bond lifetime increases until reaching a transition point, and at forces higher than this transition point, the bonds release, or “slip” (Fig. 1 E) (48).

We have modeled catch-slip bonds by assuming that attachment leads to a stress threshold that must be overcome before the attachment can be broken. The attachment of cells that undergo a catch-to-slip transition can be described by the following equation (23):

$$\frac{d}{dt}N = -N(e^{-(F/N-\phi_c)} + e^{(F/N-\phi_s)} + \gamma(N_t - N)). \quad (3)$$

Here, N_t is the total number of adhesion proteins in a cluster that can bond, and N is the number of these bonds that form attachments. F is the total force acting on this cluster, and γ is a protein-specific attachment rate. The two variables, ϕ_c and ϕ_s , describe the catch- and slip-bond terms, respectively. We consider several experimentally measured bonds, including E-cadherins, P-selectins, integrins, and fibronectins (28,29,49–51). In our model, we assume that this equation is at equilibrium, leading to a uniform number of bonds per unit length, and that each unit length of bond immediately reaches steady state upon contact, as experimentally measured bond kinetics show that E-cadherins and P-selectins reach steady state in less than 2 s (27,52,53), which is considerably faster than the time taken for the cellular deformations that we consider. Eq. 3 has two equilibria (Fig. 2 A), given by

$$F(N) = N\phi_{\max} \pm N \cosh^{-1} \left(\frac{1}{2N} e^{1/2(\phi_s - \phi_c)} \gamma (N_t - N) \right), \quad (4)$$

where $\phi_{\max} = \frac{1}{2}(\phi_s + \phi_c)$. The stable (− sign) and unstable (+ sign) solutions meet at a point at which the number of attached bonds reaches a maximum, N_{\max} , which is achieved for applied external force

$$F_{\max} = N_{\max}\phi_{\max} = N_t\phi_{\max} \frac{\gamma e^{1/2(\phi_s - \phi_c)}}{\gamma e^{1/2(\phi_s - \phi_c)} + 2}. \quad (5)$$

In our model, we take this to be a threshold determining whether the membrane is attached. To implement this threshold, we use this calculation to compute an adhesion stress threshold σ_{\max} by substituting an adhesion protein density for N_t . For example, for E-cadherin, which has $\phi_{\max} = 27$ pN, $\gamma = 5.3$ s^{−1}, and $N_t = 64$ proteins/ μm^2 , the stable and unstable solutions of Eq. 3 converge at an applied stress of $F_{\max} = 1.7$ nN/ μm^2 . We assume that the adhesion proteins are uniformly distributed along the boundary of the cell and the substrate. Then, the two-dimensional level set function is discretized onto a Euclidean grid ($dx = 0.1$ μm) to determine points of contact between the cell and the substrate. We then determine the magnitude and direction of the total stresses acting on the cell at each point of contact. We use the result from Eq. 5 as a threshold (σ_{\max}) that must be overcome to pull the cell away from the surface. For example,

$$\sigma_{\text{tot-net}} = \min(\sigma_{\text{tot}} + \sigma_{\max}, 0). \quad (6)$$

In this way, we are not modeling individual bonds but use a threshold that is based on experimentally measured, protein-specific bond density and kinetics as well as bond breakage forces. If the total stress at that point is less than the threshold of adhesion, the point remains adhered. Alternatively, if the total stress is larger, then the point detaches. Using the bond numbers described above, we found threshold values in the range of 1–5 nN/ μm^2 , which are consistent with experimental measurements of cell attachment (54,55).

Implementation of mechanics

With these parameters implemented into the viscoelastic model of cells, we can begin to dissect the machinery and stresses needed for cell-cell interactions such as those we see in entosis and other cell consumption events. Through experimental measurements using micropipette aspiration and atomic force microscopy, we know that cell mechanics can be modeled using the Kelvin-Voigt-Dashpot viscoelastic model (24,56). In particular, our viscoelastic model assumes that the cell is a compound material consisting of a mostly elastic membrane and cortex and a mostly viscous cytoplasm (Fig. 1 B). The evolution of the local deformation along the normal direction of the boundary is given by

$$\dot{x}_{\text{cyto}} = (1/\gamma_a)\sigma_{\text{tot}} \quad (7a)$$

and

$$\dot{x}_{\text{cort}} = -(k_c/\gamma_c)x_{\text{cort}} + (1/\gamma_c)\sigma_{\text{tot}}, \quad (7b)$$

where σ_{tot} is the total stress applied on the cell; x_{cort} and x_{cyto} are the local displacements of the cortex and cytoplasm, respectively; and k_c (0.098 nN/ μm^3), γ_c (6.1 nN/ μm^3), and γ_a (0.064 nN/ μm^3) are viscoelastic components of the cell describing the elasticity (k_c) and viscosity (γ_c) of the cortex and the viscosity (γ_a) of the cytoplasm. Thus, the normal velocity of the boundary is the sum of \dot{x}_{cyto} and \dot{x}_{cort} .

Computational implementation

A summary of the steps in the model is given in Fig. S3. The model was implemented and simulated using MATLAB (The MathWorks, Natick, MA) and the LSM Toolbox (43). Using the LSM Toolbox derivative function called Upwind First First (first-order upwind approximation of the first derivative), the integrator function called ode CFL1 (first-order Euler scheme with a Courant-Friedrichs-Lewy constrained time step of ~ 0.01), and a grid size (dx) of 0.1 μm , we can model ~ 1.5 biological hours per hour of computational time. On a grid size of 40×50 μm , run on a Mac-Book Pro 2.4 GHz 8-Core Intel Core i9, 1 h of simulation time resulted in a little less than an hour of biological time.

RESULTS

Modeling cell-to-substrate adhesion

We began by simulating the interaction between a spherical cell and a solid surface. To move away from its equilibrium state, a cell must experience force, which may be internally generated or externally applied. One of the smallest forces seen in a biological system arises from Brownian fluctuations. The magnitude of thermal fluctuations of the membrane has been measured experimentally using a variety of techniques, including fluorescence interference contrast microscopy (41,42). The resulting measurements indicate that a detached membrane fluctuates with a root mean-square displacement of ~ 50 nm. Using the Kelvin-Voigt portion of the mechanical equivalent circuit, we calculated the stress required to displace the membrane to the experimentally measured parameters (~ 55 pN/ μm^2 , Materials and methods). The resultant simulated fluctuations were smaller than the experimentally measured values (which only consider membranes), as our system is modeled as a compound material,

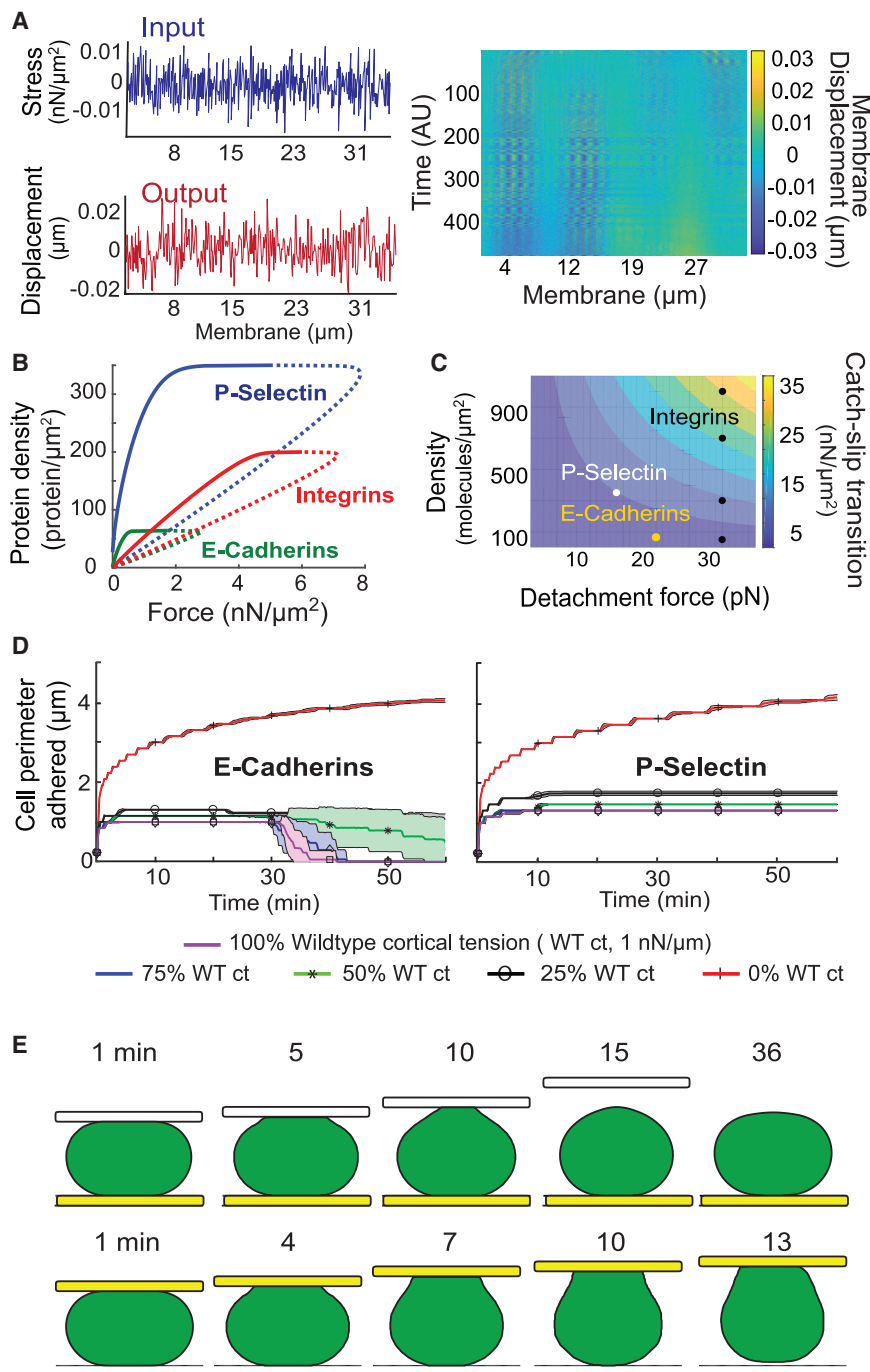


FIGURE 2 Implementation of cell-substrate adhesion. To model multicellular interactions effectively, a biologically accurate model of adhesion must be incorporated. (A) The stress required to form thermal fluctuations was used as an input to the mechanical circuit and resulted in small deformations uniformly around the cell perimeter. The kymograph illustrates the magnitude of the resulting cellular deformations across the cell boundary over time. (B) The threshold between catch and slip was determined by the intersection of the stable (solid line) and unstable (dotted line) equilibria for E-cadherin (red) and P-selectin (blue). This point represents the maximal stress on the bonds that transitions the adhesion from the catch regime to the slip regime. (C) The point of catch-slip transition varies as a function of adhesion protein density and the necessary stress to mediate the transition between catch and slip, creating an adhesion landscape. Here, the density of adhesion molecules and the detachment force of the molecules are varied in a biologically relevant regime. The color grating indicates the maximal stress the bonds can withstand before transitioning into the slip regime. Mapped to the surface are three representative catch-slip proteins (integrins at four different densities (black), E-cadherins (yellow), and P-selectins (white)). (D) Brownian fluctuations of the cell boundary allow the cell to make stochastic contact with the solid bottom surface. The amount of contact of the cell perimeter is determined by the cell-specific cell mechanics and the strength of the specific adhesion molecule (shown here are E-cadherins and P-selectins). For all tested molecules, as cortical tension of the cell decreases, we see increased cell settling, which is maintained for longer periods. Shading indicates the 95% confidence interval. (E) Cell compression simulations validate the strength of the adhesion between the cell and the substrate. When the adhesion between the bottom substrate and cell is higher (top), the cell remains attached to the bottom. In contrast, when the adhesion of the top moving beam and cell is higher, the cell will remain attached to the top beam as it moves upward with a known velocity. The surface with higher adhesion is illustrated in yellow. WT, wild-type. To see this figure in color, go online.

consisting of the membrane, cortex, and underlying cytoplasm, all of which limit the magnitude of deformation resulting from the applied stress (Fig. 2 A).

If the Brownian fluctuations were sufficiently large to instigate contact between a point on the cell perimeter and the substrate, that point would adhere. In our model, adhesion is implemented as a catch-slip bond. The lifetime of these bonds is a function of the applied mechanical load. The threshold that transitions a bond between the catch

regime and the slip regime was modeled based on an adaptation of the original Bell model (Fig. 2 B) (18,23). This formulation allows the strength, density, and kinetics to be modulated to represent diverse types of adhesion molecules increasing the flexibility of our model. We computed the adhesion landscape across a range of catch-slip adhesion molecules, which depends both on the adhesion protein density and the characteristic forces necessary for the catch-slip transition for different adhesion molecules. We found that

this implementation of integrin adhesion is linearly dependent on the density of the adhesion proteins (Fig. 2 C).

When we simulated the effect of thermal fluctuations along with catch-slip bonds, we observed moderate adhesion to the surface. In these simulations, the cell began with a single point of contact between its boundary and the surface. With a catch-slip threshold approximating E-cadherin adhesion ($1.7 \text{ nN}/\mu\text{m}^2$) and wild-type cortical tension ($1 \text{ nN}/\mu\text{m}$) (24), the bottom $1 \mu\text{m}$ of the cell perimeter adhered for $\sim 30 \text{ min}$ before the passive stresses of the cell (volume, curvature, and cortical tension) overwhelmed the bonds and detached (Fig. 2 D). We found that the amount of adhesion to the substrate was a function of the cortical tension of the cell. As the cortical tension was decreased, the fraction of the adhered cell perimeter increased, and the length of time that it remained adhered increased as well. Increasing the threshold from catch to slip of the molecular linkage, as seen in P-selectin (catch-slip threshold, $5.2 \text{ nN}/\mu\text{m}^2$), raised the extent of cell perimeter adhesion for longer periods compared to E-cadherin (Figs. 2 D and S4).

To validate the implementation of adhesion further, we simulated a cell compression experiment (55). To mimic the experimental design, the simulated cell was compressed between two solid substrates before the top surface was moved away with a known velocity (Fig. 2 E). In simula-

tions in which the adhesion between the cell and the bottom surface was $5\times$ stronger than adhesion to the top surface, the cell remained attached to the bottom, whereas the bonds broke between the top surface and the cell. Conversely, when the adhesion was stronger on the top, the cell remained adhered to the top surface after detaching from the bottom (Fig. 2 E).

Modeling active stress production

Brownian fluctuations of the cell membrane allow for stochastic contact between cells and substrates that are within proximity. These fluctuations, along with the implementation of adhesion as described above, led to some deformation but were insufficient to overcome passive cortex retraction to displace the cell significantly on flat or curved surfaces (data not shown). We next considered the role of active stresses in ensuring cell adhesion. To this end, we added a protrusive stress of magnitude $2 \text{ nN}/\mu\text{m}^2$ to the bottom $2 \mu\text{m}$ directly adjacent to areas of adhesion (Fig. S2). With the added protrusive stress, the cell deformed considerably more compared with the simulations with Brownian fluctuations exclusively (Fig. 3 A). As before, the cells began with a single point of contact between the cell boundary and the substrate. For a cell with a cortical tension of $1 \text{ nN}/\mu\text{m}$, the bottom $\sim 3 \mu\text{m}$ of the cell contacted the bottom

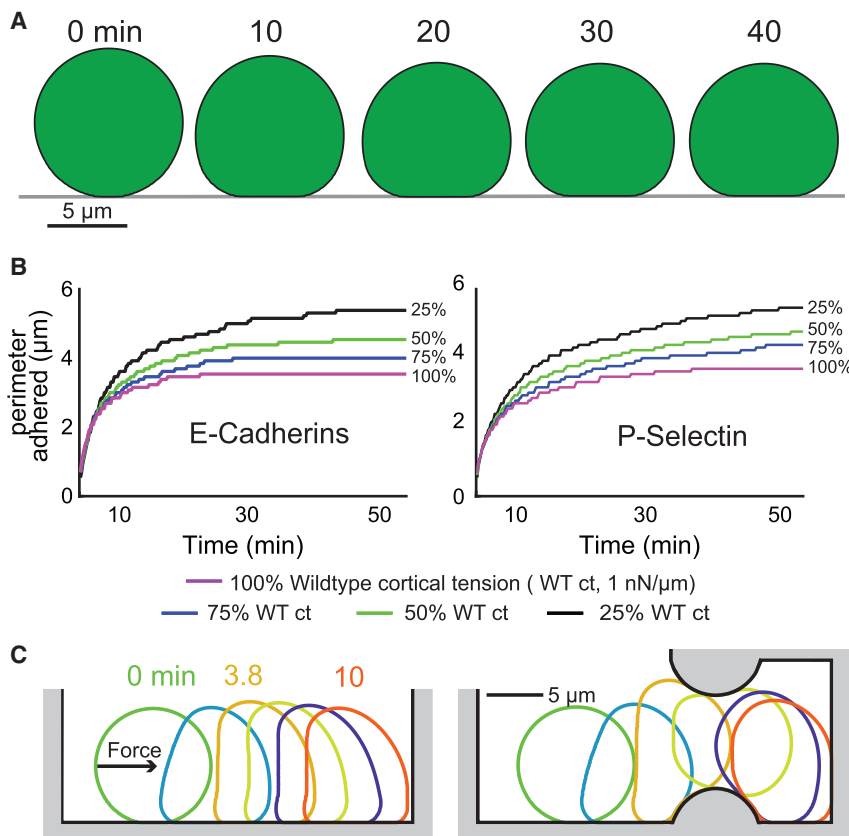


FIGURE 3 Effects of internal and external stresses on cells. The addition of active stress modeling actin polymerization results in cellular deformations. (A) A three-dimensional visualization of a two-dimensional simulation rotated about the axis of symmetry showing a cell settling with an active normal stress of $2 \text{ nN}/\mu\text{m}^2$ on the bottom $2 \mu\text{m}$ of nonadhered cell perimeter. (B) Cell perimeter contact over time for cells experiencing $2 \text{ nN}/\mu\text{m}^2$ active normal stress on the bottom $2 \mu\text{m}$ of nonadhered cell perimeter. For both E-cadherins and P-selectins, as the cortical tension of the cell decreases, the amount of cell perimeter that forms a contact with the bottom substrate increases. (C) Active normal stress can be applied to the cell in different directions to simulate varied experimental designs. Here, the stress is applied outward normal to the right. The outward normal stress was sufficient to navigate around obstacles in its path. To see this figure in color, go online.

substrate. As before, the fraction of the cell perimeter able to make and sustain contact with the surface increased as a function of decreasing cortical tension. We observed similar behaviors in the simulations of adhesion proteins with characteristics of either E-cadherin or P-selectin adhesion proteins. In fact, the deformation between these two simulations was quite similar (Fig. 3 B). Despite the difference in the strength of adhesion between these two different proteins, the magnitude of the added active stress was sufficient to overcome the passive retractive stresses that are inherent to the cell.

To simulate more diverse biological environments, we expanded the region of the cell perimeter over which these stresses are applied. To simulate a shear stress in a microfluidics-type environment, the stress can be applied outward normal to the right portion of the cell perimeter. In these simulations, the cell first was allowed to settle (as described above) and made initial contact with the bottom surface before the cell moved to the right. The environment could be made more complex by adding obstacles around which the cell had to deform (Fig. 3 C).

Interactions with solid curved surfaces

To establish the foundation of cell-cell interactions such as cell consumption events, we simulated an active cell as described above interacting with a solid passive cell. In cell engulfment events such as entosis and phagocytosis, a cell deforms around a target cell, ultimately consuming it. By testing a variety of different parameter sets, we determined a landscape of cell-cell interactions.

We first simulated active cells interacting with passive cells (more specifically, passive circular objects) of varying sizes (Fig. 4 A). In our simulations, an outer engulfing cell with a diameter of 10 μm interacted with passive cells with diameters ranging from 2 to 14 μm . We considered an outer cell generating outward normal stresses of either 3 or 6 $\text{nN}/\mu\text{m}^2$ over either 1 or 2 μm of unadhered cell perimeter (25,26). Cells that experienced higher stress over a larger region of the cell perimeter (6 $\text{nN}/\mu\text{m}^2$ over 2 μm) completed engulfment events faster than cells experiencing less stress over a smaller area (3 $\text{nN}/\mu\text{m}^2$ over 1 μm). In some circumstances (e.g., outer cells with active stresses only over the bottom 1 μm of the cell), the stress was not sufficient to complete the engulfment. Additionally, we saw that cells could consume passive cells up to an equivalent size to themselves. However, if the engulfing cell was smaller than the passive target cell, then it was unable to complete an engulfment event even at the highest stresses tested. At points of contact, the cells have adhesion with a catch-slip threshold of 1.7 $\text{nN}/\mu\text{m}^2$. For a 6 μm cell (active normal stress of 5 $\text{nN}/\mu\text{m}^2$ over the bottom 3 μm of the cell perimeter), as the size of the passive cell increased from 1 to 6 μm , the time to engulf the surface also increased from 30 to 144 min, respectively (Fig. 4 B).

We next considered the role of cortical tension during engulfment. Simulations showed that as the cortical tension of cells was reduced locally, the cells were able to complete cell consumption events more efficiently at all sizes of passive cells tested. Additionally, through this local cortical tension reduction, cells that were previously unable to complete an engulfment event were now able to with the same stress load (Fig. 4 C). For example, when the local cortical tension of the active 10 μm cell was reduced by 50%, the cell could engulf a cell of an equivalent size, whereas previously, with wild-type cortical tension, it was unable to accomplish this. This cortical tension consequence was seen most prominently in simulations containing larger passive cells. In many cases, cortical tension is proportional to viscoelasticity (57). To parse apart the role of cortical tension versus viscoelasticity, we reduced the viscoelasticity of cells independent of cortical tension (Fig. 4 D). In this scenario, the active cells engulfed the passive cells with less efficiency compared to the cells for which local cortical tension was reduced. This indicates that cortical tension resists efficient cell engulfment events more significantly than viscoelasticity.

Not all obstacles with which a cell encounters are perfectly spherical. Bacteria, for example, come in a diverse array of shapes. We therefore simulated an active cell interacting with a passive cylindrical-shaped cell to model an event that more accurately represents phagocytosis (Fig. 4 E). This simulation sets the foundation to expand the infrastructure to more cell types.

Interactions with deformable bodies

Although we successfully modeled how a cell encounters and engulfs solid objects of various sizes and shapes, we next moved to expand the biological range of our modeling framework. We incorporated deformability into the objects with which the active viscoelastic cells interacted. To this end, LSM potential functions were used for each cell. This allowed for independent modulation of the mechanics and stress production of each of the cells independently. To represent the interactions between deformable bodies accurately, we applied stresses to each cell that were proportional to the velocity of the interacting cell (Fig. 4 F). In this simulation, the engulfing cell is twofold more mechanically deformable than the cell being engulfed and is experiencing an active stress of 5 $\text{nN}/\mu\text{m}^2$ over the bottom 2 μm of non-adhered cell perimeter. This mechanical heterogeneity is often seen in successful cell-cannibalism events and is seen frequently in diseased states such as cancer (58).

With both cells having viscoelastic characteristics, we can investigate more biologically diverse and accurate cell-cell interactions such as entosis (59,60). We found that when both cells were deformable, both cells did deform in response to the stresses. With this ability to deform, less stress was needed to consume a viscoelastic cell compared with a solid cell of the same size.

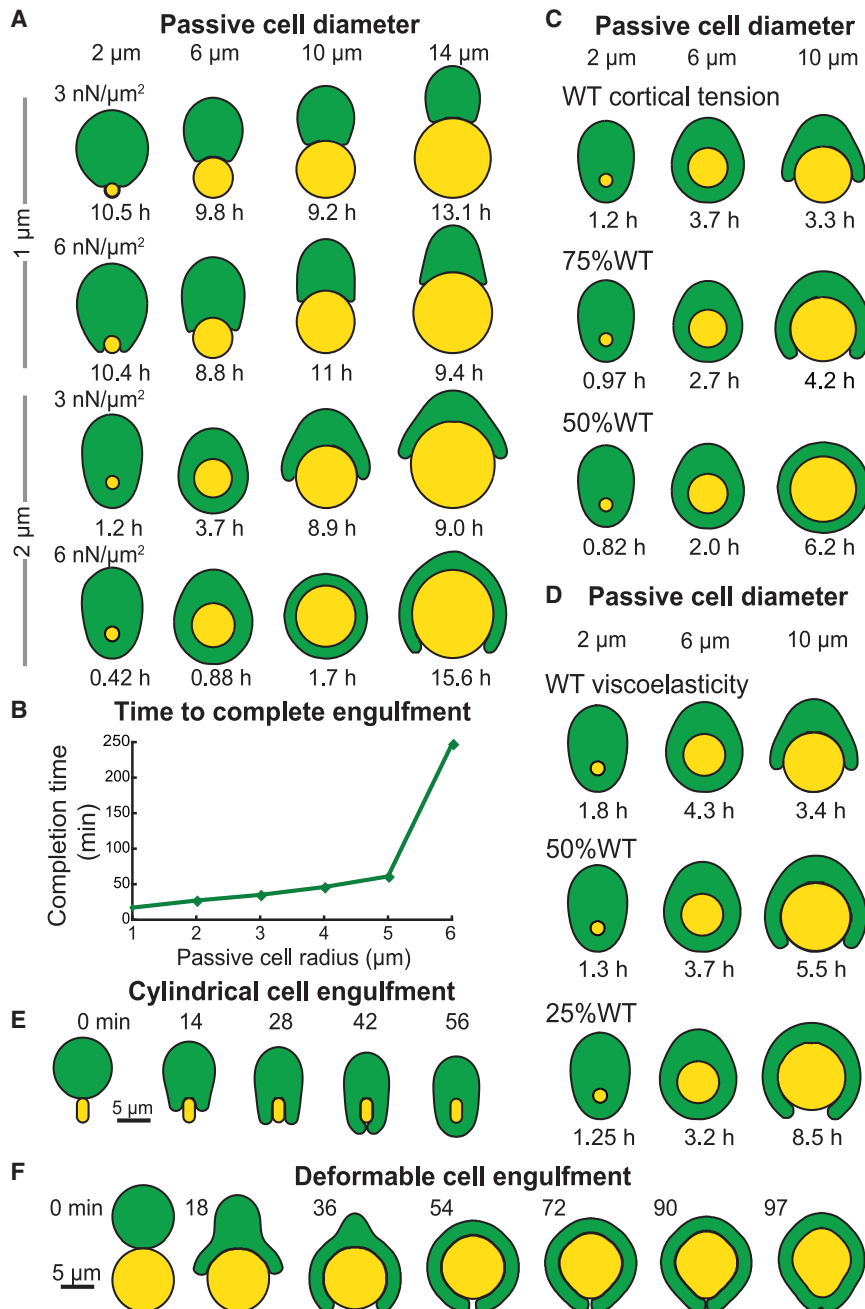


FIGURE 4 Cellular interactions with solid and deformable substrates. The addition of curvature allows for the analysis of various types of cell consumption events. (A) Landscape of cell engulfment events showing an active cell (radius 6 μm) consuming cells of varying sizes (passive cell diameter). The magnitude of the stress varied (3 $\text{nN}/\mu\text{m}^2$ or 6 $\text{nN}/\mu\text{m}^2$), as well as the size of the cell perimeter that experienced that stress (1 μm or 2 μm). (B) The time required for a cell with radius 6 μm to engulf a second passive cell of varying sizes (up to a cell of equivalent size) with a 3 $\text{nN}/\mu\text{m}^2$ stress over 2 μm . Time to completion increased almost linearly until it was challenged with a cell of equivalent size. (C) The cortical tension of the active cell was locally reduced only at regions experiencing active stress production and challenged against passive cells of varying sizes. In all instances, the cell consumption efficiency was improved with decreasing local cortical tension. (D) The viscoelasticity of the active cell was reduced independently of the cortical tension, leading to a reduced engulfment speed and fewer successful cell consumption events, especially as the size of the passive cell was increased. This indicates the effect of cortical tension more significantly affects the efficiency of cell engulfment. (E) To simulate more biologically diverse environments, we altered the shape of the passive cell with which the active cell interacted. Times of frame capture indicated above (in minutes). (F) Simulations of two active viscoelastic cells interacting with each other are shown. The green cell was twice as deformable as the yellow cell and experienced an active normal stress of 5 $\text{nN}/\mu\text{m}^2$ over the bottom 2 μm of nonadhered cell perimeter. At regions of contact, the cells applied a stress on each other proportional to their velocity. Times of frame capture indicated above (in minutes). To see this figure in color, go online.

Cellular deformations with a nucleus

In previous simulations, we assumed that the cytoplasm of the cell is a spatially homogeneous viscoelastic material. In practice, the internal compartments will greatly affect the ability to change cell shape (61). Thus, to increase the biological accuracy of the simulations, we included a deformable nucleus. To understand the effect of a deformable nucleus on cell shape, we modeled a cell settling including adhesion (threshold 1.7 $\text{nN}/\mu\text{m}^2$). We see that with a stress of 8 $\text{nN}/\mu\text{m}^2$ on the bottom third of the cell perimeter, the cell flattens, adhering to the surface leaving

room for the nucleus in the center of the cell body (Fig. 5 A). Owing to its size, the nucleus is often the limiting factor to cellular deformation especially in confined environments (61). We found that when an active cell (radius 5 μm) includes a nucleus (radius 2 μm) and then engulfs a passive cell with a radius less than that of the active cell, the nucleus did not impact the time required to complete engulfment (cf. Fig. 4 A vs. 5 B).

We also considered how the presence of a stiff nucleus affected cell deformability. To this end, we simulated the movement of a cell (radius 5 μm) into a confined space

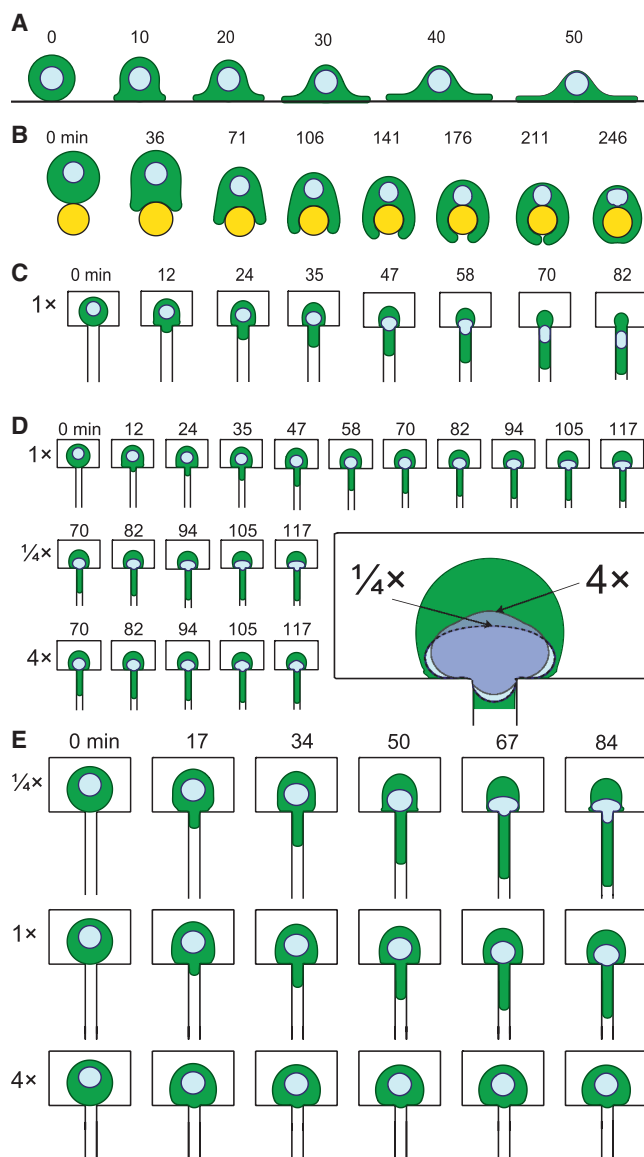


FIGURE 5 Cell shape change including a deformable nucleus. The addition of a deformable nucleus provides insight into multibody interactions within a single cell. (A) An adherent cell, radius $5\ \mu\text{m}$, with a deformable nucleus, radius $2\ \mu\text{m}$, settling on a solid flat substrate (stress, $8\ \text{nN}/\mu\text{m}^2$). (B) A deformable cell, radius $5\ \mu\text{m}$, with a deformable nucleus, radius $2\ \mu\text{m}$, consumed a passive cell, radius $4\ \mu\text{m}$, in 117 min. (C) When a cell containing a deformable nucleus was challenged by a confined environment, the cell deformed into the confined chamber before the nucleus followed to match the deformation of the cell. The confinement width is $2\ \mu\text{m}$. Stress is $4\ \text{nN}/\mu\text{m}^2$ on the bottom over $3\ \mu\text{m}$ of cell perimeter. (D) By further restricting the space, the nucleus failed to deform into the confined chamber. The elasticity of the nucleus was modulated from $0.25\times$ to $4\times$ the wild-type elasticity ($\sim 70\ \text{pN}/\mu\text{m}^2$). The stiffer nucleus did not follow readily as the cell deformed into the confined environment. The confinement width was $1.5\ \mu\text{m}$, and the stress was $4\ \text{nN}/\mu\text{m}^2$ over the bottom over $3\ \mu\text{m}$ of the cell perimeter. The inset overlays the nuclear deformations of the $0.25\times$ and $4\times$ nuclei at the 117 min time point. (E) In confinement, cortical tension played an important role in a cell's ability to deform into the chamber. As the cortical tension of the cell changed from $0.25\times$ to $4\times$ the wild-type elasticity, the cell's ability to move into the chamber was reduced. To see this figure in color, go online.

($2\ \mu\text{m}$ in width) with a stress of $4\ \text{nN}/\mu\text{m}^2$ on the bottom over $3\ \mu\text{m}$ of cell perimeter. In these simulations, the nucleus was required to deform within the cell to fit through the space (Fig. 5 C). When the width of the confinement was reduced to $1.5\ \mu\text{m}$, the nucleus was unable to deform sufficiently to fit through the confined space (Fig. 5 D). Depending on the cell type, the elasticity of the nucleus can vary anywhere from 0.5 to 6 times that of the cell (49,62,63). We simulated this situation by varying the nuclear mechanical stiffness, ranging from $0.25\times$ to $4\times$ wild-type elasticity ($\sim 70\ \text{pN}/\mu\text{m}^2$). At the higher stiffness, the nucleus restricted the cell's ability to move into the confinement (Fig. 5 D). This impact was readily observed by comparing the deformation of the nucleus at the 117 min time point. Compared to the nucleus with 25% wild-type elasticity, the cell with the $4\times$ nucleus stiffness deformed considerably less. Finally, we altered the cortical tension of the cell body with a deformable nucleus (elasticity $4\times$ wild-type). These cells experienced an outward normal stress of $8\ \text{nN}/\mu\text{m}^2$ over the bottom third of the cell perimeter (Fig. 5 E). As the cortical tension of the cell increased from $0.25\times$ to $4\times$ wild-type, we saw that the cell's ability to deform is a function of cortical tension. When the cortical tension was low, the cell easily deformed into a confined environment. When we increased the cortical tension to $4\times$ that of a wild-type cell, the cell was unable to deform into the same confined environment.

DISCUSSION

This work provides a foundation for testing a variety of cellular interactions using LSM. The results from these simulations are consistent with what has been seen experimentally. For example, experimentally we saw that engulfment events of small cells and particles completed on the order of minutes (64,65), whereas large cells completed on the order of hours (59). Additionally, we have explored the cell engulfment parameters giving insight into the robustness of cell engulfment. Testing the sensitivity of the system allowed us to understand better which mechanical parameters are most responsible for successful cell engulfment events. Using cell engulfment as a testbed, we expanded our modeling framework by including a deformable cell nucleus and exploring cells in confinement and can now begin to have predictive power over diverse biological systems.

One limitation to achieving this goal using the LSM is the computational load that would be required. As previously mentioned, the computational load scales proportionally to the number of cells being simulated. In its current implementation, it would be difficult to scale these simulations to model the number of cells that are seen in other modeling techniques such as vertex models or cellular Potts models. These techniques can model systems on the order of hundreds of cells, although they lose the geometric accuracy that is achieved with the LSM (66–69). One candidate

approach to address this limitation is to use a hybrid modeling strategy with increasing degrees of course graining as one moves away from the primary cells of interest.

Our simulations demonstrate one way in which adhesion between cells or cell and substrate can be implemented in the LSM framework. Using the phase-field method, which has many similarities to the LSM (see the review (5)), there have been several implementations of both multicellular interactions (6,7) as well as cells that incorporate a nucleus (11). For example, Shao et al. incorporate adhesions through an elastic force term that acts as a drag term on cell motion (6). These bonds stretch but can break with a probability that depends on their extension. A similar approach was used by Löber et al. (7,8), who tracked a local density of adhesive sites and make the protrusive strength depend on the number of active bonds. These authors also consider the interactions between two cells by introducing two terms into the phase-field equations: one that penalizes overlap between the phase-field functions of interacting cells and another that represents adhesion by advecting the phase-field function of one cell along the normal vector to the interface of another cell. To account for the presence of a nucleus inside a cell during division, Zhao and Wang (11) incorporate two different auxiliary functions (similar to the way that we do here) and apply a steric interaction term to penalize the overlap between the cytoplasm and the nucleus. One apparent advantage of these approaches is the relative ease by which the interacting bodies can be considered. On the other hand, this is done by avoiding a sharp interface, which is one of the hallmarks of the LSM method.

The continuum models, such as the one presented here, provide an excellent platform for whole-cell simulations, although they omit details about the subcellular components. In this way, they represent a minimal model of cell shape change based on a deformable boundary. Using a mechanical equivalence circuit, all net forces and stresses are applied at this boundary, and the effect of the intracellular mechanics is incorporated through the viscoelastic model. Agent-based methods (70,71) provide an alternative approach whereby interactions between specific components are considered. Owing to their computational cost, these modeling techniques are presently limited for modeling at the cellular level except for the simplest cell types (72). Another simplification in our modeling approach is that for computational efficiency, the simulations have been done in two dimensions. One attractive feature of continuum interphase methods, such as the LSM or the phase-field approach, is that the computational steps are readily extended to deal with three-dimensional systems. This has been done in several situations when simulating other behaviors, such as cell division (10–12) or migration (73,74), in which the degree of cellular deformation is similar to those considered here. In these cases, the differences between the corresponding two- and three-dimensional models are small.

Having a solid infrastructure in place to model cellular interactions is important as we consider the role of important multicellular interactions in the body. The body is a complex system of cells interacting in predictable ways. In tissue environments, cells sense and respond to their surroundings and often change shape in response to these cues. This mechanosensation (the ability to sense and respond to mechanical stimuli) is an important part of a cell's ability to survive and maintain homeostasis in a tissue environment. Our models have focused on the mechanical modulation and stress production of a primary cell driving the engulfment of a second cell. Current literature shows that the engulfed cell can play a significant active role in cell engulfment events, as seen in processes such as entosis (59). Moving forward, we plan to interrogate the role of the engulfed cell as a driver for cell-cell interactions.

Disease states often arise when a cell loses this ability to appropriately sense and adapt to its surroundings (75). For example, in cancer, changes in cellular deformability and altered mechanoresponsive protein expression lead to aberrant cellular morphologies (62). This results in mechanical heterogeneity between cells, often causing unconventional cellular interactions. The foundation of designing an in silico tissue environment starts with a single cell-cell interaction. With the ability to model diseased tissue systems using theory and in silico methods, we could have predictive power over the system, which would help guide our future experimental design.

SUPPORTING MATERIAL

Supporting material can be found online at <https://doi.org/10.1016/j.bpj.2021.10.021>.

AUTHOR CONTRIBUTIONS

K.T.D., P.A.I., and D.N.R. designed the study. K.T.D. wrote software and ran the simulations. P.A.I. and D.N.R. acquired funding. K.T.D., P.A.I., and D.N.R. wrote and edited the manuscript.

ACKNOWLEDGMENTS

We thank the members of the Robinson and Iglesias labs, particularly Sayak Bhattacharya, for their fruitful discussions and insight over the course of the project.

This work was funded by the National Institutes of Health/National Institute of General Medical Sciences, grant/award number GM66817, and Defense Advanced Research Projects Agency, grant/award number HR0011-16-C-0139. This research project was conducted using computational resources at the Maryland Advanced Research Computing Center.

REFERENCES

1. Chang, K. C., D. F. Tees, and D. A. Hammer. 2000. The state diagram for cell adhesion under flow: leukocyte rolling and firm adhesion. *Proc. Natl. Acad. Sci. USA*. 97:11262–11267.

2. Bhatia, S. K., M. R. King, and D. A. Hammer. 2003. The state diagram for cell adhesion mediated by two receptors. *Biophys. J.* 84:2671–2690.
3. Nagai, T., and H. Honda. 2009. Computer simulation of wound closure in epithelial tissues: cell-basal-lamina adhesion. *Phys. Rev. E Stat. Nonlin. Soft Matter Phys.* 80:061903.
4. Noppe, A. R., A. P. Roberts, ..., Z. Neufeld. 2015. Modelling wound closure in an epithelial cell sheet using the cellular Potts model. *Integr. Biol.* 7:1253–1264.
5. DiNapoli, K. T., D. N. Robinson, and P. A. Iglesias. 2020. Tools for computational analysis of moving boundary problems in cellular mechanobiology. *Wiley Interdiscip. Rev. Syst. Biol. Med.* 13:e1514.
6. Shao, D., H. Levine, and W.-J. Rappel. 2012. Coupling actin flow, adhesion, and morphology in a computational cell motility model. *Proc. Natl. Acad. Sci. USA.* 109:6851–6856.
7. Löber, J., F. Ziebert, and I. S. Aranson. 2014. Modeling crawling cell movement on soft engineered substrates. *Soft Matter.* 10:1365–1373.
8. Löber, J., F. Ziebert, and I. S. Aranson. 2015. Collisions of deformable cells lead to collective migration. *Sci. Rep.* 5:9172.
9. Winkler, B., I. S. Aranson, and F. Ziebert. 2019. Confinement and substrate topography control cell migration in a 3D computational model. *Commun. Phys.* 2:82.
10. Poirier, C. C., W. P. Ng, ..., P. A. Iglesias. 2012. Deconvolution of the cellular force-generating subsystems that govern cytokinesis furrow ingression. *PLoS Comput. Biol.* 8:e1002467.
11. Zhao, J., and Q. Wang. 2016. Modeling cytokinesis of eukaryotic cells driven by the actomyosin contractile ring. *Int. J. Numer. Methods Biomed. Eng.* 32:e02774.
12. Li, Y., and J. Kim. 2016. Three-dimensional simulations of the cell growth and cytokinesis using the immersed boundary method. *Math. Biosci.* 271:118–127.
13. Herant, M., V. Heinrich, and M. Dembo. 2006. Mechanics of neutrophil phagocytosis: experiments and quantitative models. *J. Cell Sci.* 119:1903–1913.
14. Wolgemuth, C. W., and M. Zajac. 2010. The Moving Boundary Node Method: a level set-based, finite volume algorithm with applications to cell motility. *J. Comput. Phys.* 229:7287–7308.
15. Shi, C., C.-H. Huang, ..., P. A. Iglesias. 2013. Interaction of motility, directional sensing, and polarity modules recreates the behaviors of chemotaxing cells. *PLoS Comput. Biol.* 9:e1003122.
16. Barsegov, V., and D. Thirumalai. 2005. Dynamics of unbinding of cell adhesion molecules: transition from catch to slip bonds. *Proc. Natl. Acad. Sci. USA.* 102:1835–1839.
17. Buckley, C. D., J. Tan, ..., A. R. Dunn. 2014. Cell adhesion. The minimal cadherin-catenin complex binds to actin filaments under force. *Science.* 346:1254211.
18. Bell, G. I. 1978. Models for the specific adhesion of cells to cells. *Science.* 200:618–627.
19. Niessen, C. M., D. Leckband, and A. S. Yap. 2011. Tissue organization by cadherin adhesion molecules: dynamic molecular and cellular mechanisms of morphogenetic regulation. *Physiol. Rev.* 91:691–731.
20. Borghi, N., M. Sorokina, ..., A. R. Dunn. 2012. E-cadherin is under constitutive actomyosin-generated tension that is increased at cell-cell contacts upon externally applied stretch. *Proc. Natl. Acad. Sci. USA.* 109:12568–12573.
21. Albrecht-Buehler, G. 1987. Role of cortical tension in fibroblast shape and movement. *Cell Motil. Cytoskeleton.* 7:54–67.
22. Robinson, D., Y.-S. Kee, ..., A. Surcel. 2012. 7.5. Understanding how dividing cells change shape. In *Comprehensive Biophysics* E. H. Egelman, ed., Elsevier, pp. 48–72.
23. Novikova, E. A., and C. Storm. 2013. Contractile fibers and catch-bond clusters: a biological force sensor? *Biophys. J.* 105:1336–1345.
24. Yang, L., J. C. Effler, ..., P. A. Iglesias. 2008. Modeling cellular deformations using the level set formalism. *BMC Syst. Biol.* 2:68.
25. Abraham, V. C., V. Krishnamurthi, ..., F. Lanni. 1999. The actin-based nanomachine at the leading edge of migrating cells. *Biophys. J.* 77:1721–1732.
26. Prass, M., K. Jacobson, ..., M. Radmacher. 2006. Direct measurement of the lamellipodial protrusive force in a migrating cell. *J. Cell Biol.* 174:767–772.
27. Rakshit, S., Y. Zhang, ..., S. Sivasankar. 2012. Ideal, catch, and slip bonds in cadherin adhesion. *Proc. Natl. Acad. Sci. USA.* 109:18815–18820.
28. Pereverzev, Y. V., O. V. Prezhdo, ..., W. E. Thomas. 2005. The two-pathway model for the catch-slip transition in biological adhesion. *Biophys. J.* 89:1446–1454.
29. Blann, A. D., S. K. Nadar, and G. Y. H. Lip. 2003. The adhesion molecule P-selectin and cardiovascular disease. *Eur. Heart J.* 24:2166–2179.
30. Mehta, P., R. D. Cummings, and R. P. McEver. 1998. Affinity and kinetic analysis of P-selectin binding to P-selectin glycoprotein ligand-1. *J. Biol. Chem.* 273:32506–32513.
31. Osher, S., and J. A. Sethian. 1988. Fronts propagating with curvature-dependent speed: algorithms based on Hamilton-Jacobi formulations. *J. Comput. Phys.* 79:12–49.
32. Osher, S., and R. P. Fedkiw. 2003. Level set methods and dynamic implicit surfaces. Springer, New York.
33. Mulder, W., S. Osher, and J. A. Sethian. 1992. Computing interface motion in compressible gas dynamics. *J. Comput. Phys.* 100:209–228.
34. Traynor, D., and R. R. Kay. 2007. Possible roles of the endocytic cycle in cell motility. *J. Cell Sci.* 120:2318–2327.
35. Zhang, X., and M. Mak. 2021. Biophysical informatics approach for quantifying phenotypic heterogeneity in cancer cell migration in confined microenvironments. *Bioinformatics.* 37:2042–2052.
36. Zhang, X., T. Chan, and M. Mak. 2021. Morphodynamic signatures of MDA-MB-231 single cells and cell doublets undergoing invasion in confined microenvironments. *Sci. Rep.* 11:6529.
37. Mizuno, D., C. Tardin, ..., F. C. Mackintosh. 2007. Nonequilibrium mechanics of active cytoskeletal networks. *Science.* 315:370–373.
38. Guo, M., A. J. Ehrlicher, ..., D. A. Weitz. 2014. Probing the stochastic, motor-driven properties of the cytoplasm using force spectrum microscopy. *Cell.* 158:822–832.
39. Mak, M., M. H. Zaman, ..., T. Kim. 2016. Interplay of active processes modulates tension and drives phase transition in self-renewing, motor-driven cytoskeletal networks. *Nat. Commun.* 7:10323.
40. Mak, M., S. Anderson, ..., R. D. Kamm. 2017. Integrated analysis of intracellular dynamics of MDA-MB-231 cancer cells in a 3D matrix. *Biophys. J.* 112:1874–1884.
41. Kaizuka, Y., and J. T. Groves. 2004. Structure and dynamics of supported intermembrane junctions. *Biophys. J.* 86:905–912.
42. Monzel, C., and K. Sengupta. 2016. Measuring shape fluctuations in biological membranes. *J. Phys. D Appl. Phys.* 49:243002.
43. Mitchell, I. M. 2008. The flexible, extensible and efficient toolbox of level set methods. *J. Sci. Comput.* 35:300–329.
44. Dahl, K. N., A. J. Engler, ..., D. E. Discher. 2005. Power-law rheology of isolated nuclei with deformation mapping of nuclear substructures. *Biophys. J.* 89:2855–2864.
45. Mak, M., and D. Erickson. 2013. A serial micropipette microfluidic device with applications to cancer cell repeated deformation studies. *Integr. Biol.* 5:1374–1384.
46. Jean, R. P., C. S. Chen, and A. A. Spector. 2005. Finite-element analysis of the adhesion-cytoskeleton-nucleus mechanotransduction pathway during endothelial cell rounding: axisymmetric model. *J. Biomech. Eng.* 127:594–600.
47. Alam, S. G., D. Lovett, ..., T. P. Lele. 2015. The nucleus is an intracellular propagator of tensile forces in NIH 3T3 fibroblasts. *J. Cell Sci.* 128:1901–1911.

48. Dembo, M., D. C. Torney, ..., D. Hammer. 1988. The reaction-limited kinetics of membrane-to-surface adhesion and detachment. *Proc. R. Soc. Lond. B Biol. Sci.* 234:55–83.
49. Swift, J., I. L. Ivanovska, ..., D. E. Discher. 2013. Nuclear lamin-A scales with tissue stiffness and enhances matrix-directed differentiation. *Science*. 341:1240104.
50. Wiseman, P. W., C. M. Brown, ..., A. F. Horwitz. 2004. Spatial mapping of integrin interactions and dynamics during cell migration by image correlation microscopy. *J. Cell Sci.* 117:5521–5534.
51. Kong, F., A. J. García, ..., C. Zhu. 2009. Demonstration of catch bonds between an integrin and its ligand. *J. Cell Biol.* 185:1275–1284.
52. Bayas, M. V., A. Leung, ..., D. Leckband. 2006. Lifetime measurements reveal kinetic differences between homophilic cadherin bonds. *Biophys. J.* 90:1385–1395.
53. Shashikanth, N., Y. I. Petrova, ..., D. E. Leckband. 2015. Allosteric regulation of e-cadherin adhesion. *J. Biol. Chem.* 290:21749–21761.
54. Chu, Y.-S., W. A. Thomas, ..., S. Dufour. 2004. Force measurements in E-cadherin-mediated cell doublets reveal rapid adhesion strengthened by actin cytoskeleton remodeling through Rac and Cdc42. *J. Cell Biol.* 167:1183–1194.
55. Kamprad, N., H. Witt, ..., M. Tarantola. 2018. Adhesion strategies of Dictyostelium discoideum- a force spectroscopy study. *Nanoscale*. 10:22504–22519.
56. Luo, T., K. Mohan, ..., D. N. Robinson. 2013. Molecular mechanisms of cellular mechanosensing. *Nat. Mater.* 12:1064–1071.
57. Reichl, E. M., Y. Ren, ..., D. N. Robinson. 2008. Interactions between myosin and actin crosslinkers control cytokinesis contractility dynamics and mechanics. *Curr. Biol.* 18:471–480.
58. Hamann, J. C., A. Surcel, ..., M. Overholtzer. 2017. Entosis is induced by glucose starvation. *Cell Rep.* 20:201–210.
59. Overholtzer, M., A. A. Mailloux, ..., J. S. Brugge. 2007. A nonapoptotic cell death process, entosis, that occurs by cell-in-cell invasion. *Cell*. 131:966–979.
60. Sun, Q., T. Luo, ..., M. Overholtzer. 2014. Competition between human cells by entosis. *Cell Res.* 24:1299–1310.
61. Versaevel, M., M. Riaz, ..., S. Gabriele. 2013. Cell confinement: putting the squeeze on the nucleus. *Soft Matter*. 9:6665–6676.
62. Suresh, S. 2007. Biomechanics and biophysics of cancer cells. *Acta Biomater.* 3:413–438.
63. Pajeroski, J. D., K. N. Dahl, ..., D. E. Discher. 2007. Physical plasticity of the nucleus in stem cell differentiation. *Proc. Natl. Acad. Sci. USA*. 104:15619–15624.
64. Clarke, M., U. Engel, ..., G. Gerisch. 2010. Curvature recognition and force generation in phagocytosis. *BMC Biol.* 8:154.
65. Jaumouillé, V., A. X. Cartagena-Rivera, and C. M. Waterman. 2019. Coupling of β_2 integrins to actin by a mechanosensitive molecular clutch drives complement receptor-mediated phagocytosis. *Nat. Cell Biol.* 21:1357–1369.
66. Trichas, G., A. M. Smith, ..., S. Srinivas. 2012. Multi-cellular rosettes in the mouse visceral endoderm facilitate the ordered migration of anterior visceral endoderm cells. *PLoS Biol.* 10:e1001256.
67. Osterfield, M., X. Du, ..., S. Y. Shvartsman. 2013. Three-dimensional epithelial morphogenesis in the developing Drosophila egg. *Dev. Cell*. 24:400–410.
68. Hirashima, T., E. G. Rens, and R. M. H. Merks. 2017. Cellular Potts modeling of complex multicellular behaviors in tissue morphogenesis. *Dev. Growth Differ.* 59:329–339.
69. Szabó, A., K. Varga, ..., A. Czirik. 2012. Invasion from a cell aggregate—the roles of active cell motion and mechanical equilibrium. *Phys. Biol.* 9:016010.
70. Vavylonis, D., J.-Q. Wu, ..., T. D. Pollard. 2008. Assembly mechanism of the contractile ring for cytokinesis by fission yeast. *Science*. 319:97–100.
71. Cortes, D. B., M. Gordon, ..., A. S. Maddox. 2020. Bond type and discretization of nonmuscle myosin II are critical for simulated contractile dynamics. *Biophys. J.* 118:2703–2717.
72. Mak, M., T. Kim, ..., R. D. Kamm. 2015. Multiscale mechanobiology: computational models for integrating molecules to multicellular systems. *Integr. Biol.* 7:1093–1108.
73. Moure, A., and H. Gomez. 2018. Three-dimensional simulation of obstacle-mediated chemotaxis. *Biomech. Model. Mechanobiol.* 17:1243–1268.
74. Cao, Y., E. Ghabache, ..., W.-J. Rappel. 2019. A minimal computational model for three-dimensional cell migration. *J. R. Soc. Interface*. 16:20190619.
75. Surcel, A., E. S. Schiffhauer, ..., D. N. Robinson. 2019. Targeting mechanoresponsive proteins in pancreatic cancer: 4-hydroxyacetophenone blocks dissemination and invasion by activating myh14. *Cancer Res.* 79:4665–4678.